

3 Experimental Setup and Methods

3.1 Experimental Rig

The experimental rig consists of a base structure, two sets of linear-motors connected with each other via linkage systems and carbon-fibre SD7003 wall-spanning profiles weighing each 306g. The profiles have a chord length of 120mm and a span of 450mm. The profile-tip spacing at the walls is less than 2mm on either side. Maximum static blockage in the test-section based on the frontal area was under 3%. A schematic of the test rig integrated into the Eiffel-type wind tunnel test-section at the Institute of Fluid Mechanics and Aerodynamics (TU Darmstadt) is shown in Fig. 3.1. The various components of the standard Particle Image Velocimetry (PIV) system used in the majority of the measurements are also included in the schematic.

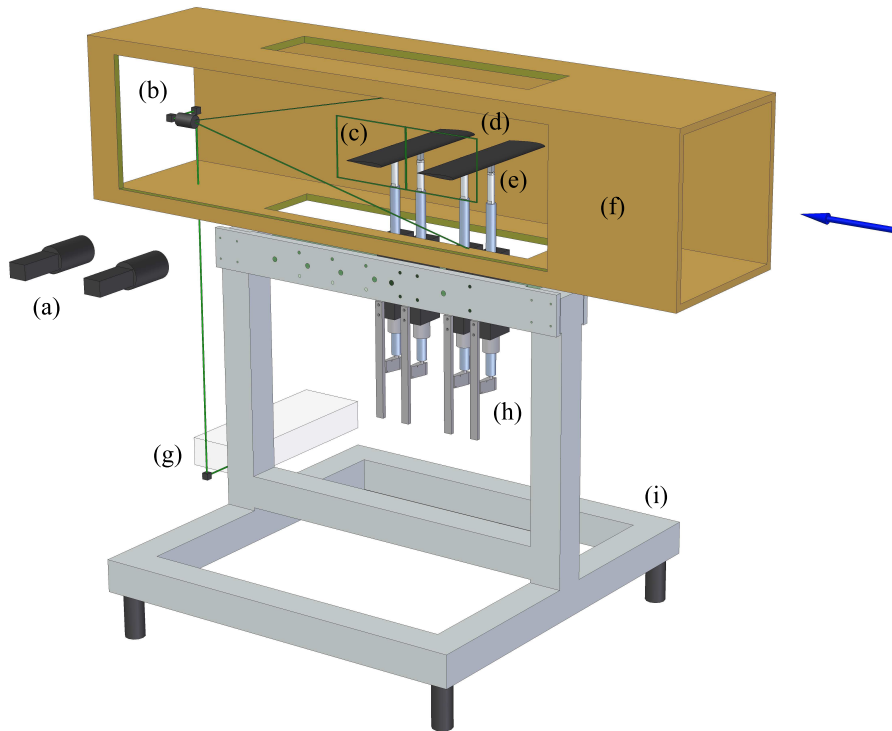


Figure 3.1: Experimental setup in wind tunnel with flow direction from right-to-left: (a) CCD cameras, (b) beam expander, (c) PIV image frames, (d) wall-spanning carbon-fibre profile, (e) embedded piezo-electric force sensors, (f) test-section, (g) laser head, (h) linear motors with linkage system and (i) base structure.

The four linear motors used to drive the pitch/plunge motion were of type LinMot PS01-48x240F-C. A displacement accuracy of $\leq 0.5\text{mm}$ was achieved in the setup depending on the duration of the experiment and the temperature of the bushings. The control of the linear motors was achieved with a combination of digital inputs for high-speed triggering and a serial port communication. A LabView 8.2 control program was developed to operate the communication system with the linear motors. Setup and

configuration of the motors was done via LinMot's own configuration and test program (LinTalk). Additional external position sensors were mounted on the motor units for higher positional accuracy, allowing for a dynamic angle-of-attack accuracy of less than 0.5° .

3.2 Profiles

3.2.1 SD7003 Profile

The airfoil selected for the wind-tunnel measurements was the asymmetric SD7003 profile as it demonstrated relatively good performance at transitional Reynolds numbers. The profile, with a maximum thickness of approximately $0.09c$, can be considered as a representative bird inner-wing profile. The point of rotation is located at the $x = c/4$ position. Another attractive feature in using the SD7003 profile is the substantial experimental database available in the open literature, both for the steady case, as investigated by Selig et al (1995) and Ol et al (2005), and for unsteady kinematics, as reported on by Nerger et al (2003), Lian et al (2008) and Ol et al (2009).

This profile has a static-stall angle of approximately $\alpha = 11^\circ$ at $Re = 60000$, as measured by Selig et al (1995) and Rival and Tropea (2009), which has been used to characterize the point where the flow reattachment process begins. The use of the static-stall angle to characterize the start of the reattachment process is supported through the experiments of Niven et al (1989).

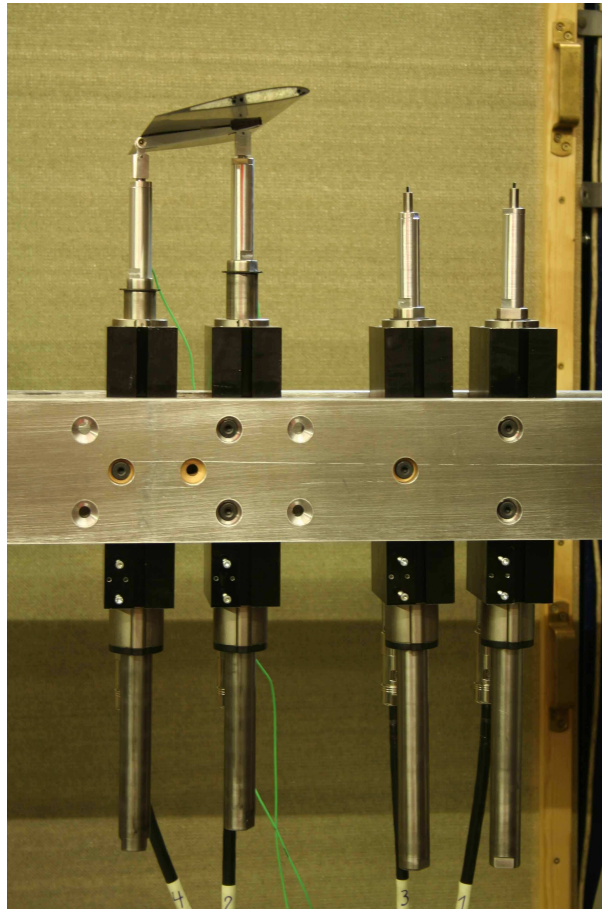


Figure 3.2: One of two SD7003 carbon-fibre profiles mounted on experimental rig; note piezo-electric force transducers situated just below profile. Also note rear linear motors for each profile rotate to allow for extra degree-of-freedom in kinematics.

3.2.2 Flat-Plate Profile

For the hover experiments the flow was to remain fully-separated and therefore a stream-lined profile was no longer necessary. Instead plexiglass flat plates were used with approximately $0.067c$ thickness and rounded leading and trailing edges. The point of rotation was again fixed at the $x = c/4$ position. Since maximum pitch/plunge frequencies of only $f = 1\text{Hz}$ were used for these experiments, stiffness was not a problem. A great advantage to using plexiglass for these measurements was the full optical access around the profile, as shown in Fig. 3.3. The thin shadow regions at the leading and trailing edges were eliminated using a moving-average filter during post-processing, as reported on in section 3.7.2.

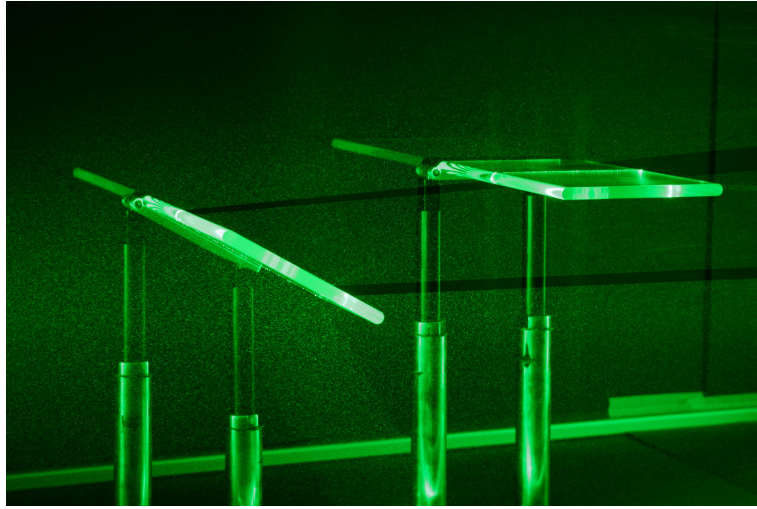


Figure 3.3: Plexiglass plates in tandem arrangement; note minimal shadows emitted from leading and trailing edges allowed for excellent optical access during PIV measurements.

3.3 Wind Tunnel

The majority of the research presented here was carried out in the Eiffel-type wind tunnel at the Institute of Fluid Mechanics and Aerodynamics (TU Darmstadt). The test section of this low-speed wind tunnel has a cross section of 45cm by 45cm and a length of 2m. Furthermore the tunnel has a contraction ratio of 24:1 with five turbulence filters in the settling chamber and produces turbulence levels on the order of 1.0% at these low test speeds. A schematic of the wind tunnel is shown in Fig. 3.4. The free-stream velocity was controlled via closed-loop control, with the tunnel speed input obtained from a hot-wire anemometer (Dantec Dynamics A/S type 55P11) positioned at the entrance of the test section. The hot-wire anemometer was calibrated for each new set of measurements using a miniature vane anemometer. In order to minimize the effects of weather on the exceptionally low tunnel speeds, the intake was modified for these studies, as reported on by Sch önweitz et al (2008), such that fresh air was sucked from within the closed hall, decoupling it from direct atmospheric influences. This modification allowed tunnel operation even in windy conditions, with a tunnel speed error of no more than $\pm 1\%$ at a tunnel speed of $U_\infty = 3.75\text{m/s}$.

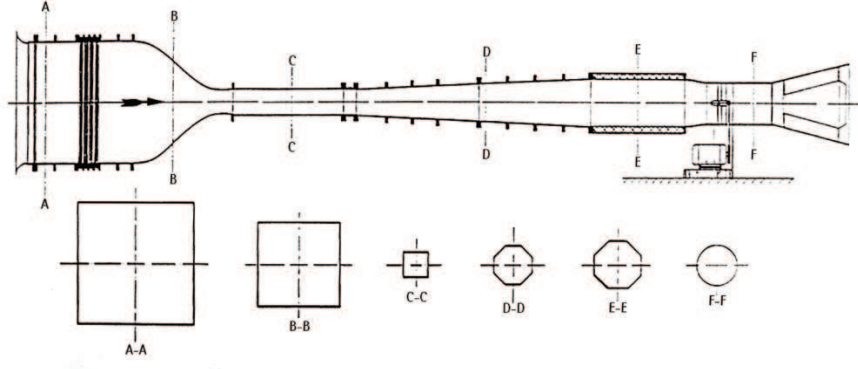


Figure 3.4: Schematic of wind tunnel; note intake (A-A) and test section (C-C) cross-sections.

3.3.1 Flow Quality

The tunnel flow quality was measured by simultaneously traversing four single hot-wire probes (Dantec Dynamics A/S type 55P11) in 50mm intervals through the test section. The measurement plane was located 800mm downstream of the test-section entrance, corresponding to cross-section C-C in Fig. 3.4 and the approximate position of the forefoil. The probe signals were fed through MiniCTA 54T30 bridges and recorded using LabView 8.2 on a 16-bit National Instruments 6259 A/D board. Sampling at each position was made over a 5s interval using a 10Hz low-pass filter. With this data turbulence intensities at the two main tunnel operating speeds were recorded, as shown in Fig. 3.5. Depicted in the plots are the boundaries of the moving airfoil as well as the PIV measurement plane.

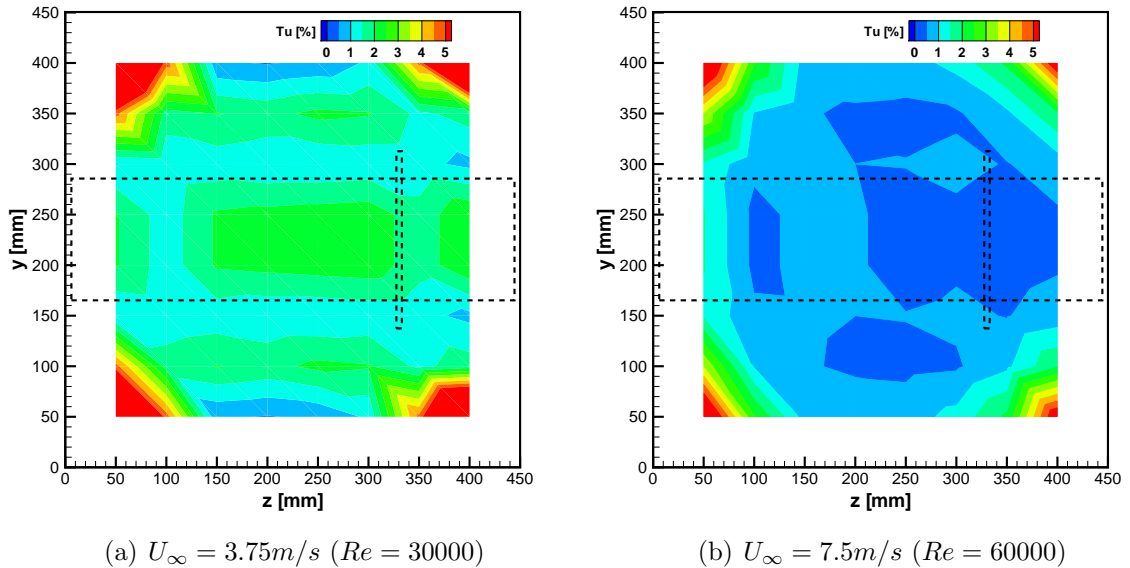
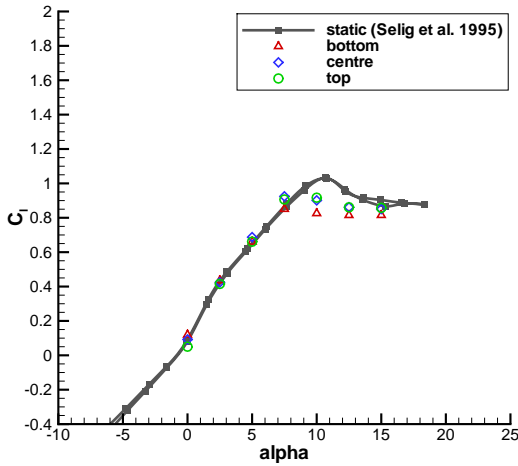


Figure 3.5: Turbulence intensities in wind-tunnel test section for the two relevant chord-based Reynolds numbers used in the wind-tunnel studies; note boundaries represent test-section walls and dashed lines the motion limits of the moving airfoil as well as the PIV measurement plane.

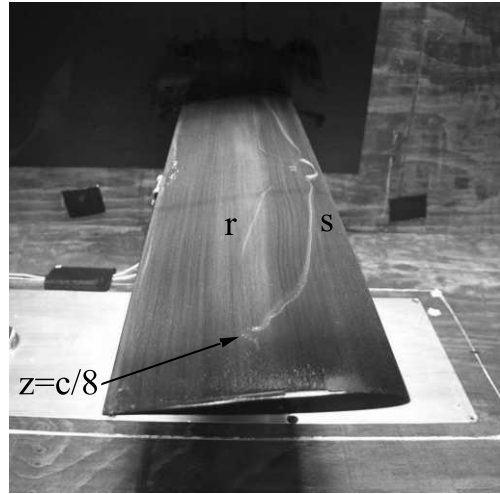
3.3.2 Assumption of Two-Dimensionality

Static Conditions

Before dynamic measurements were performed, first a thorough comparison of static measurements were made with data available in the literature. In Fig. 3.6(a) static lift measurements at various plunge positions (h) in the test section corresponding to BDC (bottom), centre and TDC (top) were made to ascertain the levels of blockage in the tunnel. Such blockage effects were found to be minimal. However, it should be noted that stall did occur earlier in the experiment when compared to the original measurements from Selig et al (1995). To determine the level of three-dimensionality found in this configuration, surface oil-flow visualizations were made using a mix of baby oil and titanium dioxide. In Fig. 3.6(b) both the laminar separation (s) and turbulent reattachment (r) lines are visualized over the span of the airfoil for $\alpha_o = 4^\circ$. It can be observed that as one moves from the center towards the tips of the profile that the laminar separation bubble shifts downstream. Furthermore, as one approaches the tip ($z = c/8$), the junction flow dominates and the separation and reattachment lines are no longer visible. It also should be noted that at the center position of the model, the waviness of the separation line was found to be an artifact of the linear motors' magnetic field on the titanium dioxide powder. Nevertheless the positioning of the struts is expected to have a local disturbance on the flow field.



(a) static lift



(b) oil visualization at $\alpha = 4^\circ$

Figure 3.6: Initial tests of SD7003 profile in tunnel at $Re = 60000$ under static conditions: (a) static lift measurements in tunnel show little variation due to vertical positioning, i.e. blockage effects are small; (b) oil-flow visualization shows clear positioning of separation (s) and reattachment (r) lines in agreement with previous experimental measurements made by Ol et al (2005).

Dynamic Conditions

Under dynamic conditions these wall-interference effects are expected to be reduced. Some of the first experimental investigations into dynamic stall using a pitching airfoil by Carr et al (1977) showed that the wing-wall interference became negligible as the reduced frequency approached $k \approx 0.1$. This was observed for tests with an aspect ratio of only 1.62, which is very low in contrast to the current investigation with an aspect ratio of 3.75. In a recent investigation by Ol et al (2009), in which a very similar

strut configuration is used to examine the pure-plunge reference cases, three-dimensional effects associated with the breakdown of the LEV are visualized using dye injection. Despite the appearance of three-dimensionality in the flow near the bottom of the stroke, there is no reason to attribute this phenomenon to wall or sting effects any more than the inherent turbulent breakdown of vortical structures.

A recent investigation by Ol et al (2009) used a very similar strut configuration to drive the same pure-plunge motion (reference case) as used in the wind-tunnel studies. Here three-dimensional effects associated with LEV breakdown were visualized using dye injection. Despite the appearance of three-dimensionality near the bottom of the stroke, there was no evidence linking this phenomenon to the facility boundary conditions. Furthermore, recent PIV measurements taken on the $x/c = 0.4$ plane normal to the free-stream direction in a similar Eiffel-type wind tunnel at TU Braunschweig confirm that wall effects are minor. Again the same pure-plunge kinematics are used, see Bansmer et al (2008) for a description of the facility. In Fig. 3.7, the spanwise flow at the bottom of the stroke for the pure-plunge reference case show spanwise flows well under 10%, and this for a relatively small aspect ratio of only 2. In light of these comparisons with other facilities as well as the strong correlations found on the PIV measurement plane (a maximum of 1% outliers for any given time step), confidence exists in the bulk two-dimensionality of the flow despite the inherent three-dimensional breakdown of the vortices shed into the wake.

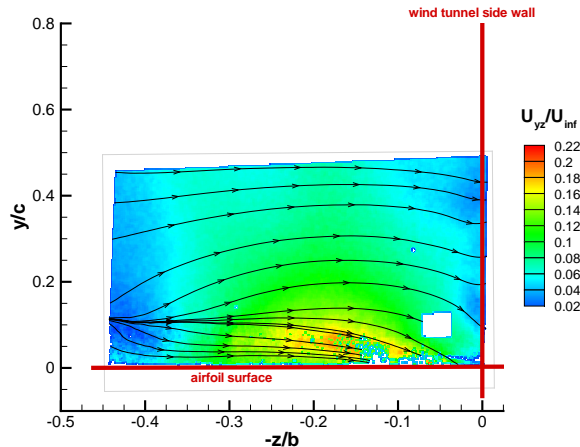


Figure 3.7: PIV measurements taken on $x/c = 0.4$ plane normal to the freestream direction in Eiffel-type wind tunnel at TU Braunschweig depicting spanwise flow at bottom of stroke for the pure-plunge reference case; note data taken from Bansmer and Radespiel (2008).

3.4 Hover Chamber

A 120cm-long plexiglass box with a cross-section of 45cm by 45cm (equivalent to that of the wind tunnel) was used for the tandem hover experiments; note back wall was 44cm ($x/c = 3.6$) from hindfoil trailing edge. Again the tip spacing at the walls was less than 2mm on both sides, thus approximating an infinite-span. Seeding was injected 30s prior to the experimental run in order to allow for quiescent initial conditions. In Fig. 3.8, the experimental rig with hover chamber is shown with the laserhead located at left and the high-speed camera at right.



Figure 3.8: The experimental rig enclosed in the hover chamber shown with laserhead located at left and high-speed camera at right.

3.5 Force Measurements

For the direct lift and moment measurements, a pair of one-component Kistler 9217A piezo-electric force sensors were integrated directly below each profile, one at the quarter-chord position (point of rotation) and one at the trailing edge. Together the two sensors could measure both the profile's inertial and aerodynamic forces during the prescribed movement. Similar piezo-electric sensors have been used successfully for the measurement of pitching and plunging foils in a tow-tank, both for a single foil and in the wake of a cylinder, see Anderson et al (1998) and Beal et al (2006), respectively. The total static tare weight of the system (profile and linkage combined) was 394g. The analog-output charge signals from the two piezo-electric force sensors were sent through the wind-tunnel floor to a Kistler 5073A411 charge amplifier, which in turn converted the signals into an analog voltage. These voltage signals were subsequently fed into a 16-bit National Instruments 6259 A/D board. Since the physical and sting natural frequencies were on the order of 1Hz and 20Hz, respectively, the signals were finally run through a 5Hz low-pass filter in LabView 8.2 and were then further post-processed using MatLab 7.3. All lift and moment measurements were based on an ensemble of 30 clean cycles, sampled at 1kHz, where the first four cycles as well as the last cycle were cut away due to aerodynamic and inertial starting and stopping effects. In order to subtract the dynamic tare for a given pitch-plunge case, a corresponding ensemble of 30 clean cycles were measured with the wind tunnel turned off. This technique proved to be very repeatable ($< 1\%$) for the lower reduced frequencies ($k < 0.15$) where the aerodynamic contribution was always equal or larger than the inertial contribution. However, at higher reduced frequencies ($k > 0.2$) the inertial loads very quickly dominated the total measured forces and therefore the accuracy of the measurements suffered greatly since the aerodynamic contribution was less than an order of magnitude smaller than the mechanical forces. Therefore in this work only direct force and moment measurements for lower reduced frequencies and at $Re = 60000$ are presented where the accuracy was estimated to lie within $\Delta C_l = \pm 0.05$ and $\Delta C_m = \pm 0.02$, respectively. For these lower reduced frequencies the tares were performed immediately after the wind-on measurements using the same profile and not the dummy cylinder, as described in section 6.2. A more detailed

description of the problems associated with extracting aerodynamic forces from the total measured forces is presented in chapter 6.

3.6 Smoke Visualizations

Smoke visualizations were performed by evaporating baby oil on an electrically-heated, steel musical-instrument string 0.16mm in diameter, which was stretched vertically across the wind-tunnel test section. The heated wire was located at the quarter-span position, one chord upstream of the leading edge. High-speed images were recorded at 231fps using a VDS Vosskühler HCC-1000 CMOS camera with a full resolution of 1024x1024 pixels coupled with a 50mm $f/1.2$ Nikkor lens. Illumination was performed using a 500W halogen light source located directed above the plane of interest. Since the quality of the generated streaklines deteriorated at higher tunnel speeds, all smoke visualizations were performed at $Re = 30000$, corresponding to a tunnel speed of $U_\infty = 3.75\text{m/s}$.

3.7 Particle Image Velocimetry (PIV)

3.7.1 Standard PIV System

A commercial PIV system was used in this study (Dantec Dynamics A/S) and consisted of a Nd:YAG ($\lambda = 532\text{nm}$) Litron dual-cavity laser with a maximum power output of 135mJ per cavity and two 10-bit FlowSense 2M CCD cameras each with a 1600x1200pix resolution. Due to the large imaging field required, 60mm $f/2.8$ Nikkor lenses were used. In order to reduce reflections the profile was painted mat-black and monochromatic filters, with a corresponding wavelength of $\lambda = 532\text{nm}$, were installed on the lenses. The laser beam was directed over three mirrors into the test-section and expanded into a sheet approximately 2mm in thickness. This laser sheet was set parallel to the flow direction and aligned onto the airfoil quarter-span position. Due to the large imaging area of 0.0864m^2 the laser power was set to 90% for both cavities. With the use of compressed air driven through four Laskin nozzles, DEHS seeding particles less than $1\mu\text{m}$ in diameter were introduced into the settling chamber using a vertical rake aligned with the measurement plane.

PIV image pairs were sampled at 15Hz allowing for 6 phases to be recorded per cycle at $k = 0.25$. In order to construct the ensemble velocity fields of 12 phases per cycle, two staggered sets with 100 images per phase were ensemble-averaged. In all cases the first two starting cycles were removed from all ensembles. Each camera imaged a field corresponding to $x/c = 2$ and $y/c = 1.5$, with a resolution of $800\text{pix}/c$ ($6.7\text{pix}/\text{mm}$). Reflections on the model surface were strongest at the bottom of the stroke where a region $0.04c$ normal to the airfoil surface was deemed to be unreliable. Shadows and strong reflections on the pressure (lower) side required masking. Parallax effects were strongest at the top of the stroke and at this position were responsible for hiding a region $0.03c$ normal to the airfoil surface. The vector fields were calculated using an adaptive correlation with $32\times 32\text{pix}$ interrogation windows and a 50% overlap. A 3×3 filter was used to lightly smooth the vector fields in order to more clearly define the vortical structures in the wake. A local neighborhood validation using a 9×9 moving-average filter and an acceptance factor of 0.2 was employed to eliminate outliers. This, however, also had the effect of smoothing the velocity gradients, thereby thickening the shear layers.

The buffer capacity of approximately 2GB could store a maximum of 528 individual images, allowing the velocity vector field to be recorded 132 times per camera per run.

After the two starting cycles were removed, 20 recordings of each phase were captured. To attain a more accurate ensemble-averaged representation of the flow, data from five different runs of 20 cycles each were used, thus creating an ensemble average of 100 cycles. Preliminary repetition tests with relatively poor seeding and light conditions can be seen in Fig. 3.9. Even for these low-quality tests, the data with 100 repetitions was deemed adequate to eliminate the background noise and to clearly represent all major flow structures, including the vortical distribution inside the LEV and TEV. Later on in the measurement campaigns optimized seeding and lighting conditions were used, thus further improving the statistical representation of the flow with only 100 repetitions.

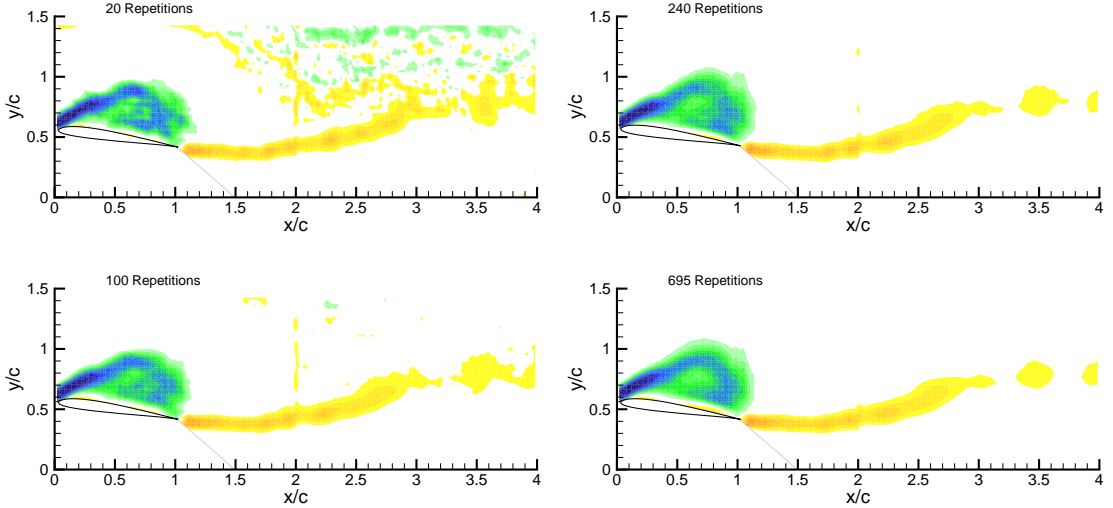


Figure 3.9: Plots of dimensionless vorticity for different ensemble sizes at $t/T = 0.333$ for the pure-plunge reference case.

3.7.2 Time-Resolved PIV System

A second PIV system incorporating a Nd:YLF ($\lambda = 528\text{nm}$) Litron dual-cavity laser with a maximum repetition rate of 10kHz per cavity was used to investigate the tandem hover configuration. The system was operated at 500Hz at its maximum output energy of 22mJ, again due to the large imaging area of 0.148m^2 . A Phantom V12 high-speed camera with 1280x800pix resolution was fitted with a 60mm $f/2.8$ Nikkor lense and was triggered in single-frame mode. The buffer capacity was 8GB, from which 3.5GB were used for the acquisition of 3500 images during seven full cycles at $f = 1\text{Hz}$. The imaging field was $x/c = 4$ and $y/c = 2.5$ in size, with a resolution of 317pix/ c (2.65pix/mm).

Parallax effects were strongest at the top of the stroke. At this position parallax was responsible for hiding a region $0.16c$ normal to the airfoil surface while at the bottom of the stroke $0.06c$ was blocked. The vector fields were calculated using an adaptive correlation with 16x16pix interrogation areas and a 50% overlap. A local neighborhood validation using a 7x7 moving-average filter with an acceptance factor of 0.05 and 5 iterations was employed to eliminate outliers and correct the shadow regions. Applying this filter affected at most 10% of the vectors.

3.7.3 Analysis and Uncertainty

Vorticity and Circulation

Vorticity was calculated by taking the curl of the velocity field using a central-differencing discretization:

$$\omega_z = \frac{\partial v}{\partial x} - \frac{\partial u}{\partial y} \quad (3.1)$$

after ensemble-averaging the velocity field over 100 cycles. Calculating the vorticity based on ensembled velocity data minimized the impact of random errors.

The circulation of the vortices was calculated from the local vorticity field using Stoke's theorem via numerical integration:

$$\Gamma = \iint_A \omega_z dA, \quad (3.2)$$

where A is the window encompassing the vortex in question. The vortices were tracked manually and the vorticity for integration was extracted from their respective windows using a threshold value of zero. As an example, the LEV and TEV windows and their respective positions at bottom dead center for the reference case are presented in Fig. 3.10.

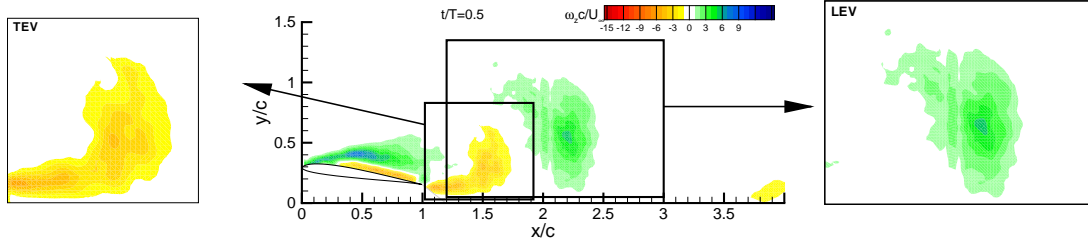


Figure 3.10: Dimensionless vorticity plot for the reference case at $t/T = 0.5$ showing the windows used to calculate the circulation of the TEV (left) and LEV (right); note no positive vorticity in TEV window and no negative vorticity in LEV window due to threshold value of zero.

It should be noted that the PIV system was only triggered once at the start of the motion with a maximum error of $\Delta t/T = 0.25\%$. After the initial external triggering the cameras and lasers would continue to take equally-spaced measurements over the cycle, with negligible error between the phases on the order of $1\mu s$.

The accuracy of the vector fields was estimated to lie well below 2% for all cases (3% for the hover configuration) assuming a maximum sub-pixel interpolation accuracy of 0.2pix , see Raffel et al (2007). Due to the coarse measurement resolution and the low vector overlap (50%), neighboring vectors were assumed to be weakly correlated. This weak correlation of the neighboring vector fields allowed for the estimation of the vorticity and circulation with uncertainties of $\Delta\omega c/U_\infty = \pm 0.5$ and $\Delta\Gamma/U_\infty c = \pm 0.05$, respectively. For more details regarding these estimates the reader is referred to Raffel et al (2007). When calculating the circulation various threshold values were tested. For a threshold of 0.1 dimensionless vorticity, a change in circulation of under 1% was measured. The largest differences were found for the TEV late in the stroke where the vortices were most dissipated. Integrating over the windows without a threshold, or using large threshold values (up to 0.5) were also tested and were deemed to not have a significant impact on the results. Therefore a threshold of zero was chosen.

The vortex trajectories were determined by tracking the approximate center of mass of the respective LEV and TEV cores in time. The spacial resolution of this manual-tracking method is approximately $x/c = y/c = \pm 0.05$.

Control-Volume Analysis

A standard control-volume analysis was used, similar to the one described by van Oudheusden et al (2007), which allowed for both a time-resolved and time-averaged comparison of the various configurations. Both lift/normal (C_l and C_n) and drag/thrust (C_d and C_t) coefficients were obtained from the force vector:

$$\vec{F}(t) = -\rho \iiint_V \frac{\partial \vec{V}}{\partial t} dV - \rho \iint_S \vec{V}(\vec{V} \cdot \vec{n}) dS - \iint_S p \vec{n} dS + \iint_S (\vec{\bar{\tau}} \cdot \vec{n}) dS, \quad (3.3)$$

where \vec{n} is the normal vector to the control surface S bounding control volume V , ρ the fluid density, \vec{V} the flow velocity vector, p the pressure and $\vec{\bar{\tau}}$ the viscous stress tensor. The unsteady term (volume integral) was neglected for the wind-tunnel measurements since large shadows limited the accuracy of the data within the volume. Nevertheless, at the relatively low reduced frequency of $k = 0.25$ used in the tunnel experiments, it was found that the unsteady term was for the most part negligible, except in the presence of strong and convective vortical structures such as the LEV in the immediate wake. At instances when the LEV or TEV passed through the control volume, discrepancies to the instantaneous forces on the order of 5% were observed when using the quasi-steady control-volume analysis. Similar results have been presented by Kat et al (2008) for the immediate wake of a square cylinder. Furthermore, when determining the average forces for a periodic motion, as presented in Table 3.1, the unsteady term cancels out over the cycle. In other words, the unsteady term is not required to determine the mean lift and drag forces.

Furthermore, to address the problem of spurious vectors due to reflections and shadows in the wind-tunnel measurements, regions of lost information on the bottom surface of the control volume (where the linear motors protruded through) were interpolated using local velocity values. Similarly the in-flow conditions assumed values of free-stream velocity and pressure. These simplifications to the control-volume analysis lead to a systematic error, which is expected to only affect the absolute force values and not the relative differences between individual cases. After lengthy comparisons, it was deemed appropriate to obtain pressure on the top and bottom control-volume surfaces based on an inviscid approach, i.e. Bernoulli. This reduced the effect of error propagation through numerical integration. The pressure on the out-flow surface, which contained strong viscous effects, was integrated using equation (3.5) based on a reference value for pressure located at the top-right of the control volume. For more details regarding this integration method see section 3.11.

An exemplary schematic depicting the position of both single and combined control volumes for the wind-tunnel measurements is found in Fig. 3.11(a). Note the single control volume was used to validate the method with direct force measurements (see Fig. 3.12 and Table 3.1) whereas the combined control volume was used for all tandem arrangements in the wind tunnel, encompassing both fore- and hindfoils. Similar to the technique used by van Oudheusden et al (2007), the corresponding uncertainty in the measured lift and drag coefficients was determined by varying the control-volume surfaces and observing the sensitivity of the resulting force coefficients. The uncertainties for the lift and drag coefficients could then be estimated to be $\Delta C_l = \Delta C_d = \pm 0.02$.

Similarly for the hover experiments, the uncertainties for the normal and thrust components were estimated at $\Delta C_n = \pm 0.05$ and $\Delta C_t = \pm 0.10$, respectively. Despite the large variation between the lift versus time distributions for the pure-plunge reference case in Fig. 3.12 and Fig. 8.5 (note two drastically different control volumes are used), the time-averaged result for lift lies within the estimated uncertainties presented above. In other words, despite the delay in convective information at the out-flow control surface for the combined control volume, the resulting mean forces can nevertheless be obtained without details of the acceleration term in Eq. 3.3.

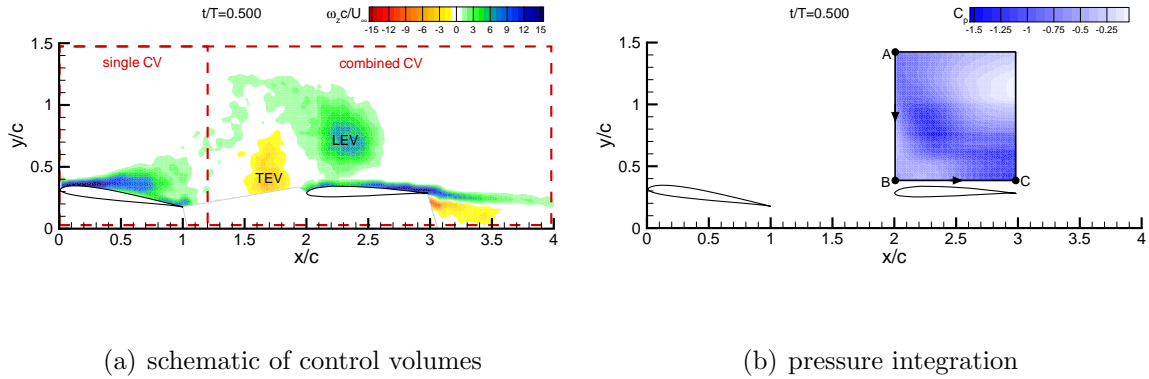


Figure 3.11: Schematics of: (a) both single and combined control volumes superimposed on top of vorticity field, and (b) pressure integration over hindfoil for pure-plunge 8° ($h/c = -0.5, 0^\circ$) case; note integration follows path A to B to C.

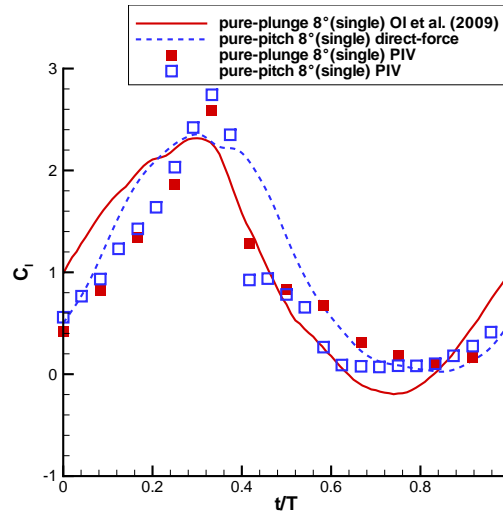


Figure 3.12: Comparison of lift forces extracted from control-volume analysis with direct-force measurements; note direct force measurements for pure-plunge 8° (single) case taken from OI et al (2009).

Pressure Integration

Due to the inherent boundary-layer separation occurring in dynamic stall and blade-vortex interactions, traditional attached-flow aerodynamics based on potential flow solutions cannot be used. Rather the rearrangement and integration of the Navier-Stokes equations (in both x- and y-directions) can provide information on the relevant pressure fields over the target airfoil:

$$\frac{\partial p}{\partial x} = -\rho \left(\frac{\partial u}{\partial t} + u \frac{\partial u}{\partial x} + v \frac{\partial u}{\partial y} \right) + \mu \left(\frac{\partial^2 u}{\partial x^2} + \frac{\partial^2 u}{\partial y^2} \right), \quad (3.4)$$

$$\frac{\partial p}{\partial y} = -\rho \left(\frac{\partial v}{\partial t} + u \frac{\partial v}{\partial x} + v \frac{\partial v}{\partial y} \right) + \mu \left(\frac{\partial^2 v}{\partial x^2} + \frac{\partial^2 v}{\partial y^2} \right), \quad (3.5)$$

where μ is the dynamic viscosity and u and v are the velocity components in the x- and y-directions, respectively. Such an analysis has been used in the past for the study of blade-vortex interaction by Wilder and Telionis (1998). Again, as mentioned above for the control-volume analysis, the unsteady terms in the pressure integration for all wind-tunnel measurements were found to play a negligible role. By integrating the Navier-Stokes equations first vertically down with equation (3.5), i.e. from points A to B from a point outside of the wake where the integration constant can be obtained through Bernoulli, the pressure near the hindfoil leading edge can be quantified. Subsequently an integration across in the streamwise direction with equation (3.4), i.e. from points B to C, is used to determine the pressure distribution over the hindfoil and thus describe the nature of the blade-vortex interaction. This integration path and the corresponding pressure field are shown in Fig. 3.11(b). The numerical integrations were performed using a forward-differencing scheme, as described by Raffel et al (2007).

The dimensionless pressure distribution obtained along line B-C was not extracted directly on the suction side of the airfoil in order to avoid integration through the optical boundary layer. The maximum deviations of the B-C integration line from the airfoil surface occur at the leading- and trailing edges and are $y/c \simeq 0.12$ for $\alpha_H = 0^\circ$ and $y/c \simeq 0.08 - 0.22$ for $\alpha_H = 8^\circ$. Once outside of the optical boundary layer, the sensitivity of the integration path was found to be minor. In order to test the level of error propagation using the pressure-integration technique, the pressure distributions were calculated by integrating vertically down towards the trailing edge and then horizontally from C to B ending at the leading edge. The maximum deviation in the pressure coefficient for all cases was approximately $C_p = \pm 0.1$. Despite the assumption of a quasi-steady flow and the error propagation associated with the pressure-integration technique, the calculated pressure distributions over the hindfoil provide the necessary qualitative insight into the nature of the low Reynolds numbers blade-vortex interactions examined in chapters 8 and 9.

Table 3.1: Validation of control-volume analysis technique for lift and drag forces; note large discrepancy in pure-plunge 8° (single) case since direct-force measurements taken from different facility, see Ol et al (2009).

case	C_l (direct-force)	C_l (PIV)	C_d (direct-force)	C_d (PIV)
static 8°	0.86	0.79	0.09	0.08
static 20°	0.84	0.88	0.33	0.28
pure-plunge 8° (single)	0.96	0.88	-	0.09